8-2019

Geometric Characterization of Polygonal Hydraulic Jumps and the Role of Weir Geometry

Taylor Edwin Nichols
Clemson University

Geometric characterization of polygonal hydraulic jumps and the role of weir geometry

---

A Thesis
Presented to
the Graduate School of
Clemson University

In Partial Fulfillment
of the Requirements for the Degree
Masters in Science
Mechanical Engineering

---

by
Taylor Edwin Nichols
August 2019

Accepted by:
Dr. Joshua Bostwick, Committee Chair
Dr. John Saylor
Dr. Richard Miller

Abstract

Hydraulic jumps are characterized by flows with an abrupt change in the fluid height, as seen in tidal basins, rivers, and dam spillways. They also occur on smaller scales and we have developed a small-scale table top experiment consisting of an impinging fluid jet impacting a horizontal plate to systematically study the geometry of the hydraulic jump. Striking polygonal shapes are observed which depend upon the flow of the impinging jet, fluid properties, weir geometry and the flow history. These steady shapes are reflective of a balance of inertial, pressure, and surface tension forces. The effect of weir height and geometry on the modal behavior and jump geometry is studied. Two experimental protocols are introduced that illustrate the effect of flow history and hysteresis in the formation of polygonal hydraulic jumps. This highlights the nonlinearity inherent in mode selection. We are able to collapse all of our experimental data with the Weber number using the downstream fluid height as the characteristic length scale. The critical wavelength is shown to be approximately constant which strongly implies the mode selection mechanism is related to Plateau-Rayleigh breakup. Our results highlight the complex multiphysics involved in this phenomena.

Acknowledgments

I would like to thank my adviser Dr. Joshua Bostwick for his motivation and guidance throughout this project allowing me to grow into a better researcher. I thank Drs. Saylor and Miller for serving on my committee and providing advice. The countless insightful conversations with my fellow researchers Jesse Bergen, Xingchen Shao, Saiful Tamim, Philip Wilson, Caleb Wilson, Bailey Basso, and Chase Gabbard have influenced new ideals and motivation for my research. I thank Dr. Daniel Fant, Steven Fredericks, Michael Murad, Chase Wentzky, Sidney Key, and Blake Smith for the assistance with designing the experimental apparatus. Lastly, I would like to thank my wife and family for the support throughout my Clemson endeavor.

Table of Contents

List of Tables

List of Figures

Chapter 1

Introduction

Hydraulic jumps are seen in a multitude of scales ranging from tidal basins [43] to kitchen sinks [54] and are characterized by a transition from a fast moving shallow flow to a slow moving deep flow. The transition between the two regimes is referred to as a hydraulic jump. The Froude number $Fr = V/\sqrt{gh}$, which is defined as the ratio of inertia to gravitational forces is used to characterize the phenomena. Upstream of the jump the inertia forces are dominant so that $Fr > 1$ and the flow is said to be supercritical whereas downstream gravitational forces dominate, $Fr < 1$, and the flow is subcritical, as shown in Figure 1.1. The decrease in velocity causes an adverse pressure gradient to develop causing flow separation which results in a sudden jump in fluid height in order to conserve mass. The hydraulic jump can be laminar or turbulent and this depends upon both the working fluid and far-field boundary conditions. For example, Figure 1.2 shows that a circular hydraulic jump can be turbulent with water but laminar with glycerine. The presence of a geometric obstruction or weir in the far field downstream region is also important and will be discussed later. On large scales the vortexes under the jump are useful by hindering erosion effects downstream of dam spillways and can also remove air entrapped in water supply and sewage lines. Hydraulic jumps are also useful in irrigation systems because of the deep slow flow in the downstream region. On smaller scales understanding the behavior of hydraulic jumps can be useful in coating flows, cooling by an impinging jet, chemical mixing, and other thin film applications [10, 57].

The typical flow structures for laminar jumps are illustrated in Figure 1.3. The simplest flow occurs in the Type 1 jump, Figure 1.3a, and consists of single change in fluid height accompanied by a vortex in the downstream region. A Type 1 jump using glycerol as the liquid is shown in

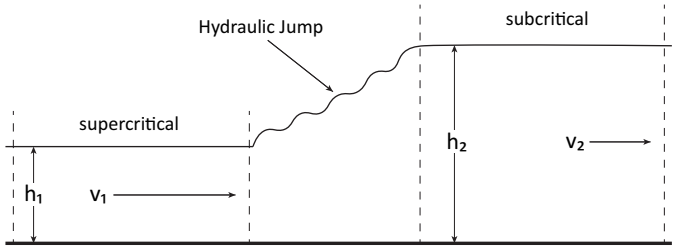

Figure 1.1: Schematic of planar hydraulic jump showing the transition from supercritical to subcritical flow.

Figure 1.2b. As the height in the subcritical region increases, there is an accompanying change in flow structure to a Type 2a jump, shown in Figure 1.3b, in which there remains a single change in fluid height and a secondary recirculation vortex develops. The Type 2b jump, Figure 1.3c, is characterized by two changes in fluid height and is sometimes referred to as a double jump [17].

(a) Turbulent circular hydraulic jump

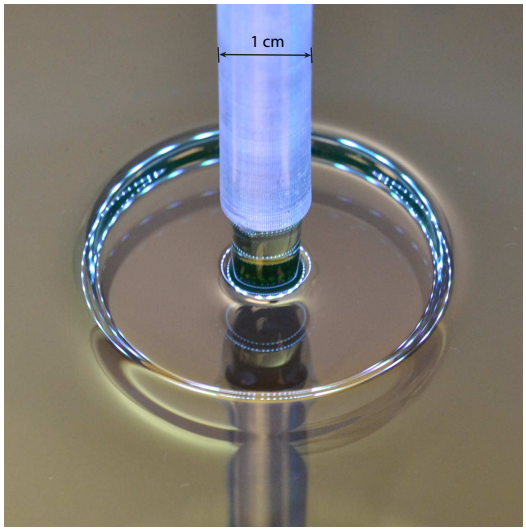

(b) Laminar circular hydraulic jump

Figure 1.2: Typical hydraulic jumps can be (a) turbulent or (b) laminar.

Figure 1.4 provides a schematic of the relevant forces involved for a laminar Type 1 hydraulic jump. The jump interface has a radius of curvature and surface tension forces F_γ directed towards the center of curvature while the vortex introduces a force F_ω towards the fluid interface. Gravitational forces F_g are directed upstream while the upstream and downstream velocities give rise to inertia forces F_{v_1} and F_{v_2}, respectively. Lastly, viscous forces F_η resist flow near the wall and at the rollers where flow stretching occurs.

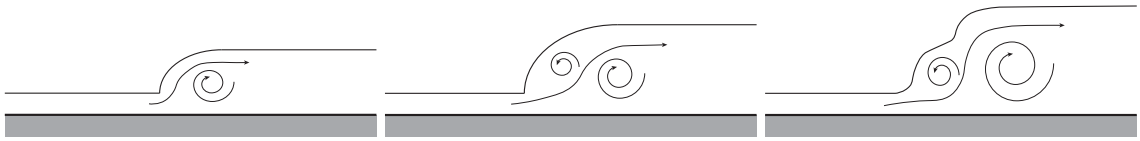

(a) Type 1 (b) Type 2a (c) Type 2b

Figure 1.3: Schematic of the different flow regimes (a) Type 1, (b) Type 2a, (c) Type 2b, in laminar hydraulic jumps. Type 2 (b,c) is characterized by an additional secondary recirculation vortex, with Type 2b (c) distinguished by a double jump structure.

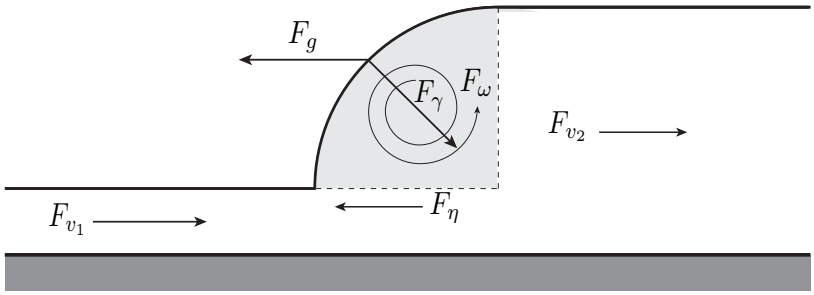

Figure 1.4: Flow schematic of Type 1 hydraulic jump illustrating the relevant forces.

1.1 Circular hydraulic jump

One of the earliest studies of hydraulic jumps was given by Rayleigh 1914 [43] who developed an inviscid theory in planar coordinates to describe the flow conditions upstream if the downstream conditions are known. The theory also showed that energy across the jump is not conserved more than likely a consequence of viscous dissipation. Although no experiments were performed, Rayleigh stated this phenomenon could be studied in more detail by the means of an impinging jet impacting a horizontal plate. One of the first experimental studies was conducted by Tani 1949 [48] who identified the flow separation and eddy recirculation just downstream of the jump. Birkhoff et al. [3] extended Rayleigh's results and developed an inviscid theory to predict the jump radius for circular jumps appearing by an impinging jet on an horizontal plate. Watson [54] incorporates viscous effects to predict jump radius in circular hydraulic jumps by introducing a boundary layer in the supercirtical region for both laminar and turbulent flow conditions. Watson compared his own data with the model along with a number of other experimental studies [36, 23, 35, 8, 13, 19, 51], and the results showed varying agreement with the model. There have been numerous other experimental studies of hydraulic jumps [32, 16, 10, 1, 40, 28, 29, 24, 30, 47]. Improvements to these models were made by including surface tension effects as was first mentioned by Bowles and

Smith [9], and Liu and Lienhard [32] who introduced non-dimensional groups such as the Weber number. Notably, Bush and Aristoff [11] developed a model that generalized the model of Watson to include surface tension and showed it accurately predicted a large experimental data set. This is one of the more recognized models and fits experimental data well. A variety of mathematical methods and simulations have been developed over the years to describe the pressure, boundary layer, inertia, and surface tension to model the flow structure, height profile, or location of the jump [9, 4, 21, 16, 22, 5, 6, 55, 10, 56, 40, 57, 20, 53, 11, 41, 28, 27, 58, 50, 46, 45, 38, 52].

1.2 Polygonal hydraulic jumps

As mentioned earlier, the introduction of a geometric obstruction (weir) in the downstream region can affect the hydraulic jump structure. Ellegaard et al. [17] [16] observed striking steady polygonal shapes, as shown in Figure 1.5, by introducing a circular weir downstream of an impinging liquid jet. These structures are characterized by a mode number N identified by the number of sides of the polygon and have similar flow structures to those shown in Figure 1.3c. Steady polygonal jumps are observed in an extensive experimental study by Bush et al. [12], along with the identification of a clover regime, which exhibits structures such as 3 and 4-leafed clovers and butterfly patterns, among others. They identify the range of parameters for these structures and show the polygonal jumps are related to the Plateau Rayleigh instability of a liquid column [39, 42]. Teymourtash and Mokhlesi [49] observed rotating polygonal jumps for higher downstream weir heights. The existence of these striking structures are not only limited to smooth horizontal plates but also have been observed on micro-decorated surfaces [14], on micro-patterned surfaces [26], and on rotating surfaces [25]. A phenomenological model is presented by Martens [33] to predict the jump shape, which further supports findings that the polygonal structures are related to the Rayleigh-Plateau instability. Inertial lubrication theory has been used to predict both circular and polygonal structures [46, 45, 44]. A more detailed theoretical study of the flow structure, particularly the vortices, has been conducted by Labousse and Bush [31]. Figure 1.6 illustrates the flow in a polygonal jump. The flow from the impinging jet is directed outward into the rotating vortex at the jump. The particle then works its way outwards until it gets accelerated into the subcritical flow. Figure 1.6a shows the rotating vortexes at the corners and Figure 1.6b show that the flow is directed outwards into the subcritical flow.

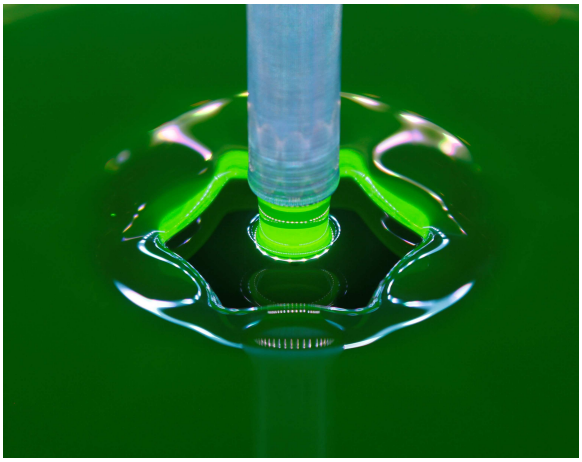

Figure 1.5: Steady $N = 6$ sided polygonal hydraulic jump.

1.2.1 Motivation

This thesis is concerned with characterizing the geometric structure of polygonal hydraulic jumps, as it depends upon i) the weir geometry and ii) the flow history.

Prior experimental studies of polygonal hydraulic jumps have generally neglected the effect of weir geometry and in circular jumps the results have been somewhat inconclusive. Craik et al. [13] has stated that the downstream flow conditions don't impact the hydraulic jump upstream in progressive studies. Experimental studies conducted in [54, 51] adjust the jet Reynold's number, weir height, and nozzle radius concluding that the jump radius is a function of the jet Reynold's number and the nozzle diameter. Geometric effects on impact plates without a weir are studied by Brechet and Neda [10], who show that laminar jumps are unaffected by geometry, whereas turbulent jumps are affected by micro-patterned [26] and micro-decorated [14] surfaces. Most studies of polygonal hydraulic jumps utilize large impact plates (36cm in diameter) such that the weir is sufficiently downstream so as to not affect the jump. This thesis addresses this issue. This information will be useful in the future development of mathematical models to explore the physics of polygonal hydraulic jumps.

Polygonal hydraulic jumps are known to exist in a particularly small region of the relevant parameter space and the specific jump geometry largely depends upon the flow history. As such, it is critically important to establish detailed experimental protocols. Here we establish two unique protocols; 1) upscale-downscale and 2) natural state. The first protocol exhibits strong hysteresis in the observed mode number as it depends upon the flow rate. The second protocol identifies an

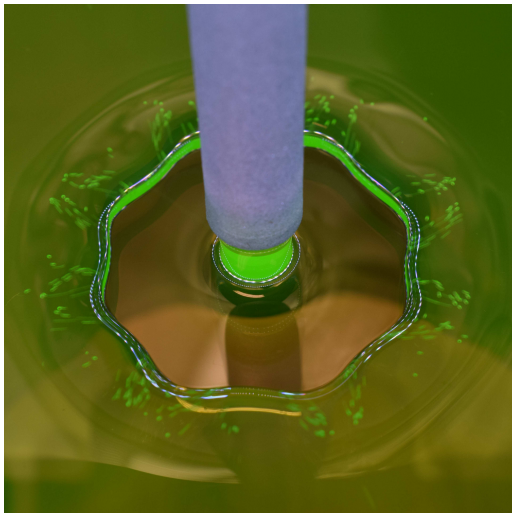

(a) Path of a particle in polygonal hydraulic jump.

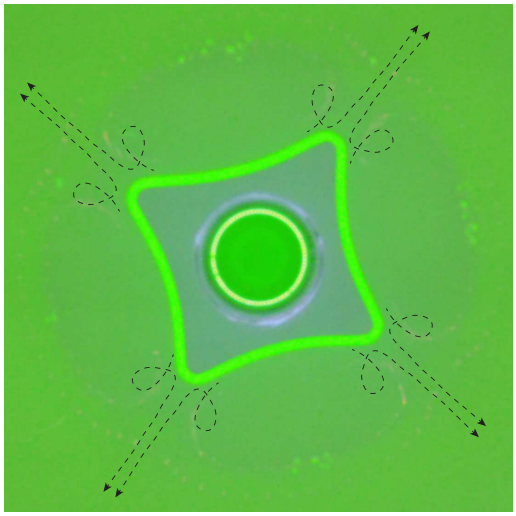

(b) Air entrap in the rotating vortexes in the corners.

Figure 1.6: Type 2b flow visualization in polygonal hydraulic jumps. The particle paths are illustrated sub-figure in 1.6a and the rotating vortexes in the corners sub-figure in 1.6b.

optimal shape preferred by the system, but in some cases there can exist multiple preferred states.

The models for polygonal structure lack information regarding the geometry of the jump resulting in simplifications of the forces responsible for creating these structures. In previous experimental studies for polygonal structures the area and perimeter of the supercritical region is never found. In this study image processing techniques are utilize to elucidate this information.

Chapter 2

Experiment

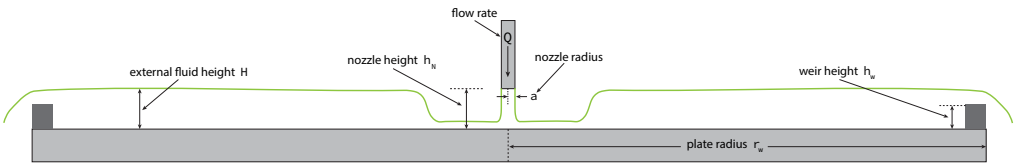

Figure 2.1: Schematic of the hydraulic jump showing a liquid jet impacting a plate with a weir of height h_w affixed at the outer edge of the plate r_w.

Experiments are performed by pumping a viscous fluid at flow rate Q through a nozzle of radius a at a height h_N onto an impact plate, as shown in Figure 2.1. After the fluid impacts the plate it flows radially outward over a weir of height h_w located at the plate radius r_w and into a catch tank, which is then recirculated through the system in a closed loop. In our experiments, the weir is always located at the edge of the plate so as to create the 'free-fall effect'. The liquid typically forms a hydraulic jump, but this is not always the case. To properly study the effects of weir geometry h_N and a are kept constant throughout the experiments and h_w, r_w, and Q are varied. By adjusting the weir height h_w and flow rate Q the external height of the fluid H changes and in a small range of parameters a striking polygonal structure can appear (Fig.1.5). The range of parameters explored in these experiments are shown in 2.1.

Parameter	range
nozzle height (h_N)	1.0 [cm]
nozzle radius (a)	0.46 [cm]
flow rate (Q)	$(30 - 110)$ [mL/s]
weir height (h_w)	$2.67 - 3.4$ [mm]
external fluid height (H)	$5.50 - 6.52$ [mm]
weir radius (r_w)	$7.62 - 17.78$ [cm]

Table 2.1: Range of experimental parameters.

2.1 Experimental Setup

The experimental setup consists of a circulation tank, impact plate and weir, nozzle, pump setup, cross member, flow meter, height measurement device, and imaging platform as shown in Figure 2.2. Precise control of the experimental conditions is needed to achieve steady polygonal hydraulic jumps. In what follows, we describe in detail the steps required to produce these steady shapes.

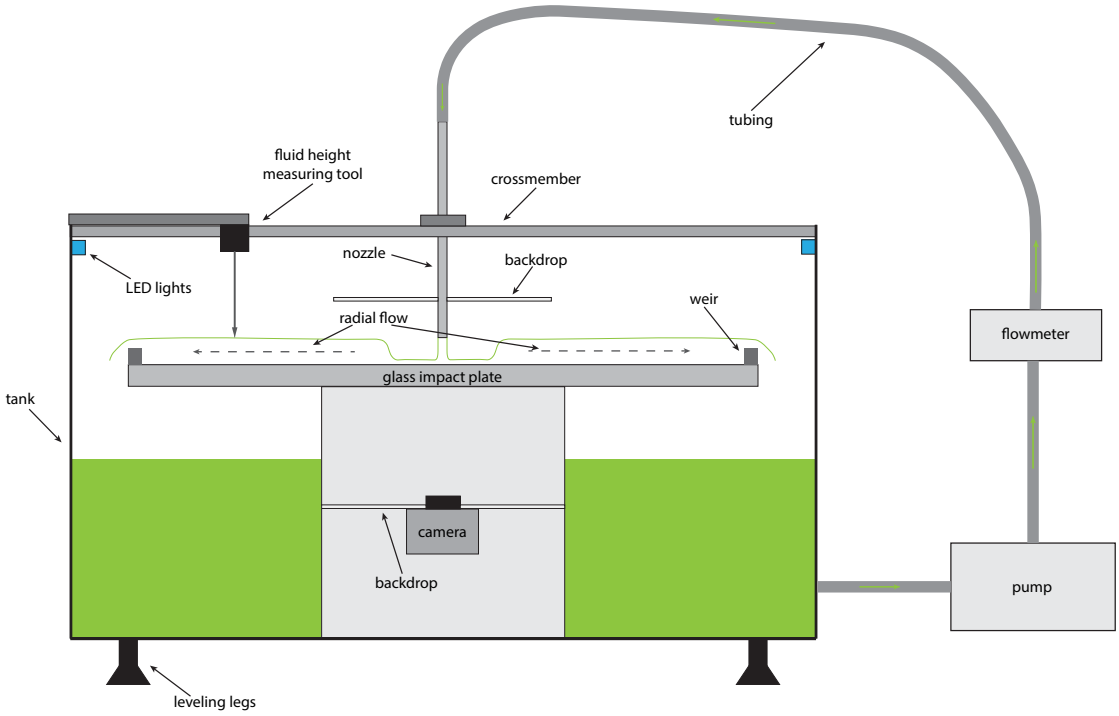

Figure 2.2: Schematic of the experimental setup

Multiple points of adjustments are implemented to ensure the impinging jet is orthogonal

to the impact plate. By using three leveling legs on the tank and a DXL360S dual axis digital protractor the impact plate can be leveled to an accuracy of 0.01°. Similarly the nozzle can be oriented orthogonal to the impact plate by using an adjustable nozzle mount. In previous work polygonal jumps were accomplished with nozzle radii $a = 0.2\text{cm} - 0.515\text{cm}$ in [6, 18, 12, 49]. Tapered nozzle designs were used to reduce turbulence and encourage uniform flow [12, 49]. Recommendations by McCarthy and Molloy [34] Bergthorson et al. [2], are provided to design a nozzle to produce a uniform velocity profile but this is difficult to achieve over the entire range of flow parameters used here. Tests were performed with both uniform and tapered nozzles and the flow was qualitatively similar in all cases. To ensure that all velocity profiles were fully developed and laminar an uniform nozzle design using recommendations from Durst et al. [15] was used. Glass is used for the impact plate because it is flat, has uniform thickness, and allows for easy imaging of the jump from underneath. Weirs of varying geometry are glued to the outer edge of the impact plate. The goal of this work is to investigate the effect of weir geometry and we used four circular plates of radius $7.62\text{cm}, 12.7\text{cm}, 15.24\text{cm}, 17.78\text{cm}$ and a square plate with edge length 22cm. For each geometry, we used 4 separate weir heights $h_w = 2.67\text{mm}, 2.84\text{mm}, 3.17\text{mm}, 3.4\text{mm}$ that were precision manufactured by a 3D printer. Small imperfections in the weir height along the circumference were noted to cause asymmetries in the jump structure. To resolve this issue, we used fine grit sand paper to ensure the weir height was uniform which we measured with digital calipers to within 0.01mm. In total, we conducted experiments on 16 weir geometries

The fluid height measurement tool allows for the downstream fluid height H to be measured. A stepper motor translates a threaded rod with a needle mounted at the end up and down. With an electrical current running through the fluid, the height of the fluid is registered once the needle point recognizes electric contact. For all experiments the height is measured 3cm inside the edge of the weir. This method is also utilized by Ellegaard et al. [16] and Rao and Arakeri [40]. Through experimentation it is found that H is uniform at a distance $> 5\text{cm}$ downstream from the jump.

A steady, pulseless flow is required to achieve steady polygonal jumps and we use an Iwaki MD-30RT-115NL centrifugal pump. We note that we tried using a diaphragm pump but were unable to produce polygonal jumps due to the high degree of pulsing. The flow rate is adjusted using a variac allowing for fine adjustments of $\approx 1m\text{L/s}$. The flow meter consists of a Digiten FL-408 paddle sensor calibrated for each fluid by conducting a bucket test to reveal the relationship between paddle frequency and flow rate. This shows a maximum error of $1m\text{L/s}$. Following previous studies ethylene

glycol (EG) is used as the working fluid [49, 12, 17] . Commercial anti-freeze solutions were used and the density, viscosity, and surface tension were measured using an Anton Paar DMA 35, Anton Paar MCR 302 rheometer, and CSC tensiometer, respectively. Those properties are given in Table 2.2. We note the pump temperature tended to increase over time which could affect the fluid properties during a given experiment. A pump cooling system was implemented to maintain the liquid at room temperature.

Fluid	ρ [g/cm^3]	η [mm^2/s]	σ [mN/m]
anti-freeze	1.12	13.7-16.4	44

Table 2.2: Fluid properties of working fluids at room temperature $23°C$. Density ρ in g/cm^3, viscosity η in mm^2/s, and surface tension σ in mN/m

The geometric structure of the hydraulic jump is captured by a camera that is mounted underneath the impact plate, as shown in Figure 2.2. The YI-4k camera can be controlled wirelessly which allows for operation in this location. To provide a consistent background and reduce unwanted light, white backdrops are mounted around both the nozzle and camera. LED lights are mounted inside the tank facing inwards to illuminate the jump.

2.2 Image Processing

Previous literature has either neglected or simplified the specific geometry of the polygonal hydraulic jump, despite the critical need for both interpretation of experimental results and the development of mathematical models. It is the explicit goal of this thesis to reveal the details of the geometric structure in the supercritical region of the hydraulic jump. This will be accomplished through identification of the area A and perimeter P.

The image processing technique is schematically illustrated in Figure 2.3. An image is captured from beneath the hydraulic jump and the center of the picture was found by recognizing the impinging jet, using a Matlab function that finds circles within a range of predetermined pixels. The image is then cropped to a reasonable size and centered as shown in Figure 2.3a. The green matrix is separated from the RGB matrix in Figure 2.3b where the strong green accent is shown by the brighter pixels. A filter is used to binarize the image resulting in the outline of the hydraulic jump shown in Figure 2.3c. Next white pixels are used to fill in everything inside the outline and black pixels outside the outline resulting in Figure 2.3d from which the area A can be computed. An

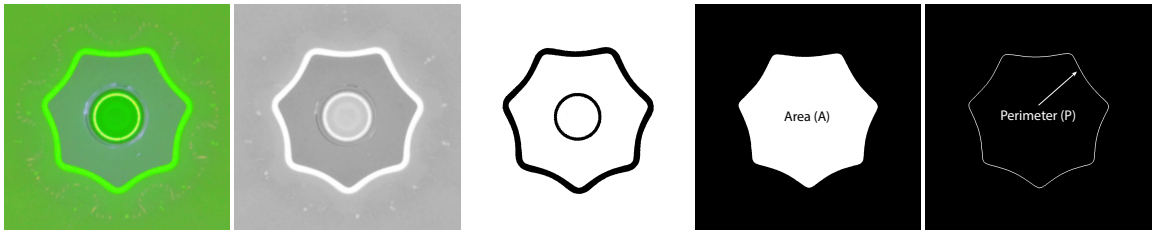

(a) cropped image (b) green matrix (c) filtered image (d) area image (e) perimeter image

Figure 2.3: Image processing protocol takes a raw image 2.3a that is filtered 2.3c from which the area 2.3d and perimeter 2.3e can be computed.

edge detection algorithm is used on Figure 2.3d to yield Figure 2.3e from which the perimeter P can be calculated. By counting the white pixels from Figure 2.3d and 2.3e and using a predetermined relationship of A in mm^2 to number of pixels, and P in mm, the geometry of the supercritical region can be found.

A calibration is done to relate the number of white pixels in Figures 2.3d and 2.3e to area A and perimeter P respectively. To do so shapes with similar attributes and magnitudes to those seen in the experiments are created in SolidWorks. Polygonal shapes with concave and convex sides, and round corners of modes $N = 3 - 9$. 25 of these shapes ranging from the smallest area to the greatest area seen in the experiments are then printed to a 1:1 scale. Since SolidWorks allows for A and P to be known, these values are then linked to their respective shapes. These shapes are then placed on the impact plate and pictures are taken the way they would be during experiments. From these pictures the respective pixels for A and P is found. With these pixels values known and the actual A and P known a relationship can be found.

2.3 Dimensionless groups

We will describe our data using three dimensionless groups; The Reynolds number $Re \equiv Q/\eta a$ for the liquid jet represents the effect of inertia over viscous forces. The Weber number $We \equiv \rho Q^2/\gamma H^3$ is the ratio of inertia to surface tension forces and the Bond number $Bo \equiv \rho g a^2/\gamma$ the ratio of gravitational to surface tension forces. For all the experiments $B = 5.28$. The mode number N and characteristic ratio A/PH are shown to correlate with the Reynolds number Re and the geometry of the jump collapses upon scaling with We. The characteristic ratio A/PH characterizes the geometry of the jump and the flow. The area A and perimeter P are primarily influenced by inertia

and viscous dissipation as the flow rate Q increases inertia and equivalently A, as seen experimentally in radial flow hydraulic jump studies [54, 36, 13, 51, 32, 16, 10, 11, 12, 28, 29, 50, 30, 49]. Larger area A in the supercritical region generates more viscous dissipation. The height of the fluid H affects both surface tension and gravitational forces. As H increases so does the gravitational force, and the surface tension force decreases because its inversely proportional to radius of curvature. Accordingly, the characteristic ratio A/PH informs us about both the geometry of the jump and the relative magnitude of forces there. The mode number N is represented by the number of sides and is used to observe transitional behavior. The hysteresis ΔRe quantifies the robustness of a given shape N and highlights the nonlinearity of the problem. The scaled wavelength λ/H is related to the mode number $\lambda = P/N$ and defines the instability mechanism.

Parameter variable	range
characteristic ratio (A/PH)	$0.3 - 2.4$
mode number (N)	$3 - 10$
Reynold's number (Re)	$450 - 1350$
hysteresis (ΔRe)	$100 - 525$
Weber number (We)	$150 - 1180$
wavelength ratio (λ/H)	$100 - 525$
Bond number (B)	5.28

Table 2.3: Dimensionless groups and the range of parameters in experiment.

2.4 Experimental Protocol

A given set of parameters will yield a polygonal jump shape that is not necessarily unique and depends upon the path towards that set of conditions. Otherwise stated, hysteresis is possible and highlights the nonlinearity in this problem. The experimental protocol is important and we describe three such techniques; i) upscale-downscale, ii) natural state, and iii) forced, in this section. In each case, the flow rate is adjusted in $1 - 2m$L/s increments during the experiments.

2.4.1 Upscale-Downscale

The upscale-downscale experiment finds the range of parameters for which a mode number N is possible. The maximum and minimum Re values allows the robustness of a given shape N to be quantified. The protocol is as follows. The flow rate is slowly increased from the lowest possible flow

rate where a steady jump appears. This is usually the $N = 3$ shape. The flow rate is then increased in small increments typically $(1 - 2)m$L/s. At each increment data is collected which includes flow rate, external height, and a picture is taken. It is important to note that the hydraulic jump isn't physically interfered with so that natural transitions from $N \to N + 1$ will occur. This process is continued until the jump becomes unsteady. This typically occurs with modes $N = 9$ or $N = 10$ and completes the upscale experiment. The downscale portion of the experiment starts at the maximum flow rate found from the upscale portion. The procedure is identical but the flow rate is decreased at prescribed increments. This procedure allows for the lower bound of the polygons to be found. The flow rate is decreased until the hydraulic jump collapses in on the fluid jet.

2.4.2 Natural State

The natural state is defined as the preferential configuration of the jump at a given flow rate Q. The protocol differs from the upscale-downscale in that the jump structure is destroyed by a probe at each increment in flow rate. This interference destroys the jump and allows for another structure to naturally form and settle. Data is then collected for that structure and the process is repeated increasing the flow rate by a small increment. It is important to use small increments because the transition from polygons $N \to N + 1$ does not always happen suddenly, and under certain conditions there are multiple shapes N that can exist for that particular flow rate. We repeat the process until modes appear unsteady.

2.4.3 Forced

Our largest weir $h_w = 3.4$mm does not produce steady polygonal jumps using either the upscale-downscale or natural state protocols. However, steady jumps can be obtained by alternative means which we call forced. There is no particular protocol to conduct this experiment and whenever a steady structure appears a data point is collected. The methods include random creation, physical obtrusion, varying the flow rate, or some combination thereof. Typically steady structures occur around $Q = 80 - 110$ mL/s at which point random high mode numbers appear. The flow rate is then decreased rapidly and typically the structure will settle at a random N. Repeating this multiple times and with careful adjustments of the Q, a considerable data set can be collected. Though this method is not ideal it can still produce some useful information.

Chapter 3

Experimental Results

This chapter reports our experimental results on polygonal hydraulic jumps and is organized as follows. We begin by reporting the mode number N as it depends upon the Reynolds number Re for both the natural state and upscale-downscale protocols. Typical mode shapes are shown in Figure 3.1. For the upscale-downscale protocol, there is a range of flow conditions under which a particular mode N is excited that depends upon the direction of the flow increment and we characterize this hysteretic range by ΔRe. Next, we characterize the polygonal jump geometry through the characteristic ratio A/PH which collapses the data for a particular weir geometry, irrespective of the experimental protocol. We then show how this ratio depends upon the weir height and weir radius. That ratio depends strongly on the weir height, but is independent of the weir radius up to a critical ratio of nozzle diameter to plate diameter. Lastly, we collapse our entire data set using the Weber number and show that the critical wavelength of the polygonal shape approaches a constant value which suggests the instability is related to surface tension effects and the Plateau-Rayleigh instability of a liquid column.

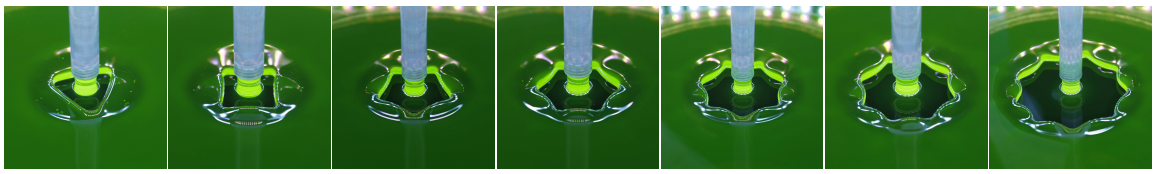

Figure 3.1: Experimentally observed polygonal jumps exhibit mode numbers $N = 3 - 9$.

3.1 Mode number N selection

3.1.1 Natural state results

Figure 3.2 shows the results of a typical natural state experiment where the mode number N is plotted against the Reynolds number Re. Increasing Re leads to an increase in mode number N and that trend appears to be linear. Interestingly, for the higher mode numbers, multiple shapes are capable of being excited for a given Re. For example, Figure 1.2 shows that for $Re = 800$, it is possible to excite a $N = 7$, $N = 8$, or $N = 9$ mode. That is, mode selection is not unique, despite the fact that the natural state protocol requires the destruction of the previous polygonal structure and the relaxation of the jump into the new state. We assume that these regions correspond to the boundary of the domain of attraction between two or more mode shapes.

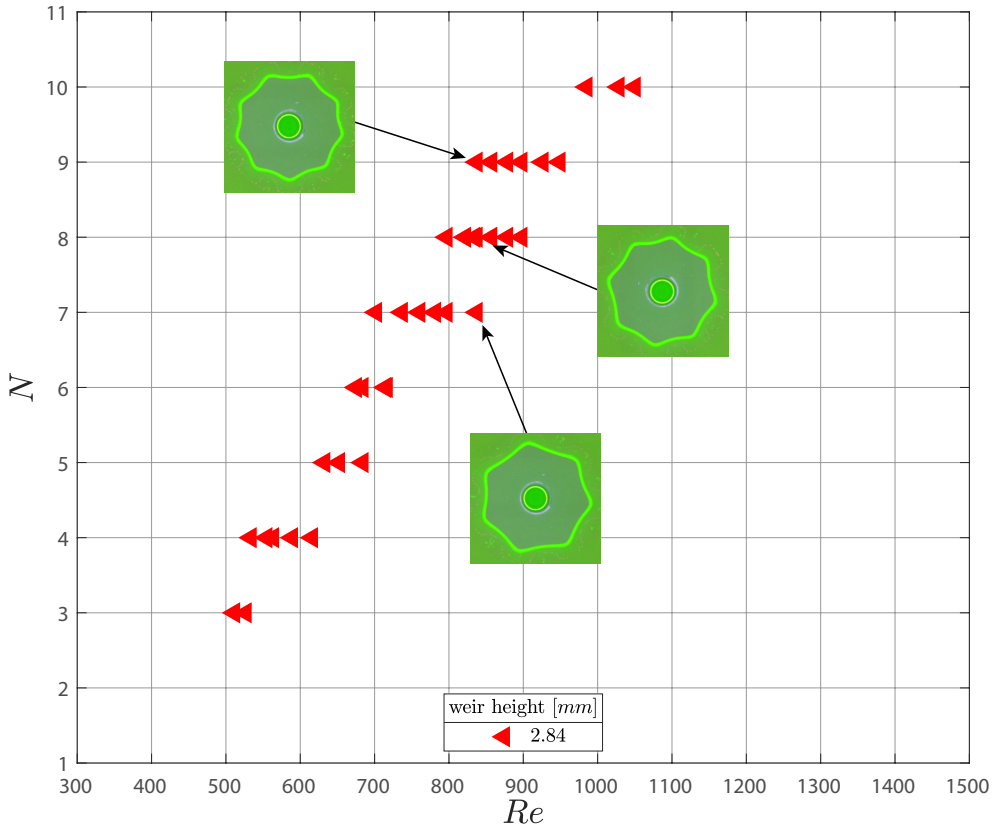

Figure 3.2: Mode number N against Reynolds number for the $h_w = 3.17$mm weir on the $r_w = 17.8$cm plate for the natural state protocol.

The goal of the natural state protocol is to observe the polygonal jump with lowest energy and the overlapping behavior of Re is more than likely due to natural and experimental perturbations introduced. The flow in the supercritical and subcritical regions must be tranquil and any small perturbation would cause a transition. We observed this phenomena in experiment and were careful not to disturb the flow. Lastly, we note that asymmetry in the jumps wasn't common in the natural state experiments but did occur and more frequently in the regions where different N would overlap.

3.1.2 Upscale-downscale and hysteresis

Figure 3.3 plots the mode number N against Reynolds number Re for a typical weir in an upscale-downscale experiment. During the upscale sweep, modal transitions occur when $N \rightarrow N+1$ and during the downscale sweep when $N \rightarrow N-1$. For a given mode N, the upscale and downscale transition occur at different Re and this difference increases with mode number N. For example, $N = 7$ begins at $Re = 930$ during and upsweep and $Re = 700$ on a downsweep. This difference illustrates hysteresis in this phenomena, a feature synonymous with nonlinearity. Our data allows for a quantitative method to represent the robustness of the modes. The maximum Re for a given mode N is found during the upscale sweep of the experiment and the minimum Re can be found during the downscale sweep and the difference between these values we refer to as the hysteresis ΔRe, as shown in Figure 3.3. At any Reynolds number Re more than one mode can exist and for $700 < Re < 900$ there are four potential modes. Two examples of these modes are shown as inset of Figure 1.3 for $Re = 550$ and $Re = 930$.

As the Re increases for a fixed mode number N the area A and perimeter P of the shape will increase and the shape will transition from $N \rightarrow N+1$. Immediately before the modal transition, one or more sides of the polygon either become asymmetric or convex and at that point the shape transitions, as shown in Figure 3.4a. Note that the lower mode number $N = 3-6$ tend to have concave sides before the transition, whereas the higher mode number $N = 7-9$ tend to be asymmetric before they transition. During the downscale sweep the sides are typically concave and the shape decreases in size as the Re decreases. Once the corners become close enough such that the rotating vortices interact with one another the corners collapse and the shape transitions from $N \rightarrow N-1$, as shown in Figure 3.4b.

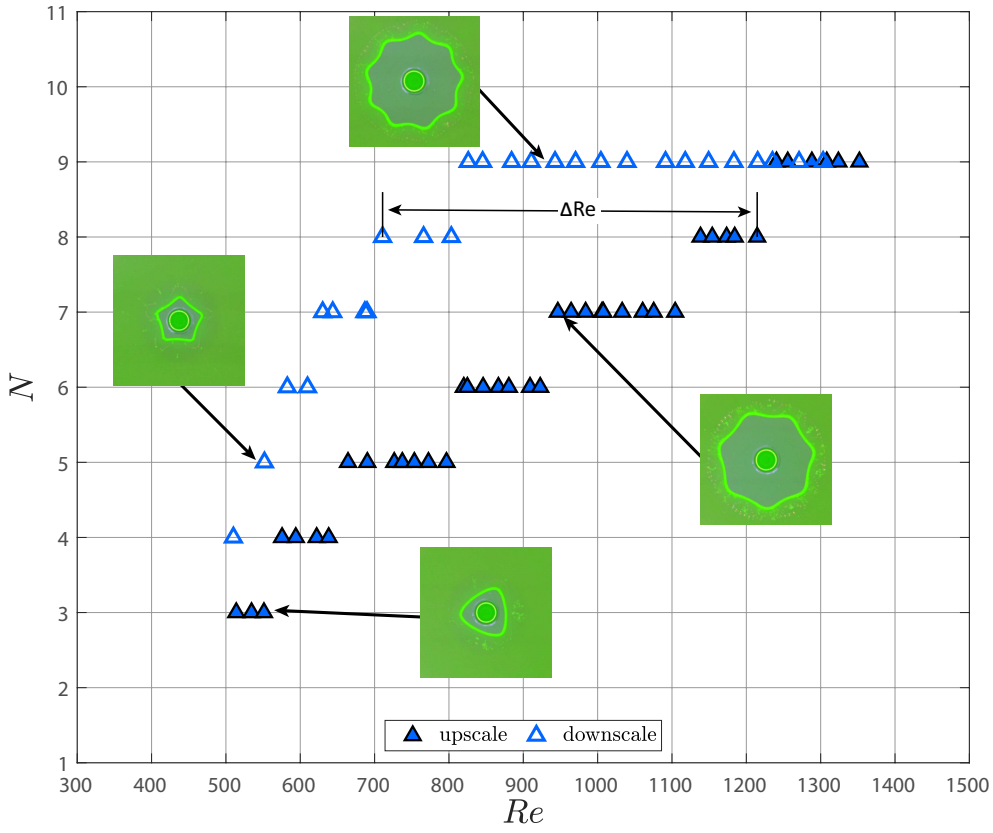

Figure 3.3: Mode number N against Reynolds number for the $h_w = 3.17$mm weir on the $r_w = 17.8$cm plate for the upscale and downscale experiments. Upscale and downscale data are given by closed and open symbols, respectively. At Reynold's $Re = 550$ a $N = 3$ mode appears in the upscale and a $N = 5$ mode in the downscale [inset]. Upscale and downscale data are given by closed and open symbols, respectively. The mode hysteresis ΔRe is defined as the range of Re where a given mode appears and is shown for the $N = 8$ mode.

3.1.3 Forced

For our largest height $h_w = 3.4$mm weir, we are not able to attain steady polygonal shapes using the upscale-downscale or natural state protocols. However, we are able to produce steady jumps using the forced method protocol discussed in Section 2.4.3. Figure 3.5 plots the mode number N against Reynolds number Re for this data, which is shifted towards higher Reynolds number when compared with our next tallest $h_w = 3.17$mm weir shown in Figure 3.3. This implies more inertia is required to attain a given shape on the taller weir, as could be expected. Interestingly, steady polygonal jumps exist over a wide range of parameters, as shown in Figure 3.5. For given Re, there

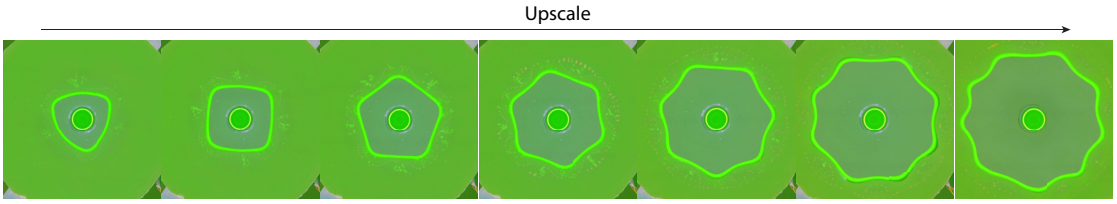

(a) Maximum state for mode numbers N

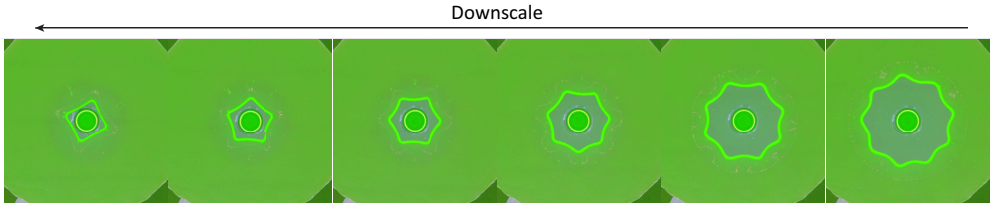

(b) Minimum state for mode numbers N

Figure 3.4: Mode transition during upscale-downscale experiment for the $h_w = 3.17$mm weir on the $r_w = 17.78$cm plate. The particular Reynolds number Re where the transition occurs can be seen in Figure 3.4b.

are many regions where four modes can exist and some small regions where even five modes can exist. This phenomena was not observed for the other weirs.

Figure 3.6 shows a montage of steady polygonal modes with the same $Re = 690$. The corners of each polygon have similar radius of curvature, which is different than observations made with the other weirs and as the mode number N increases the sides become more concave. This could mean that gravitational effects or vortex inertia are restricting the surface tension forces from causing a transition $N \to N + 1$. This could also be why none of the sides are convex.

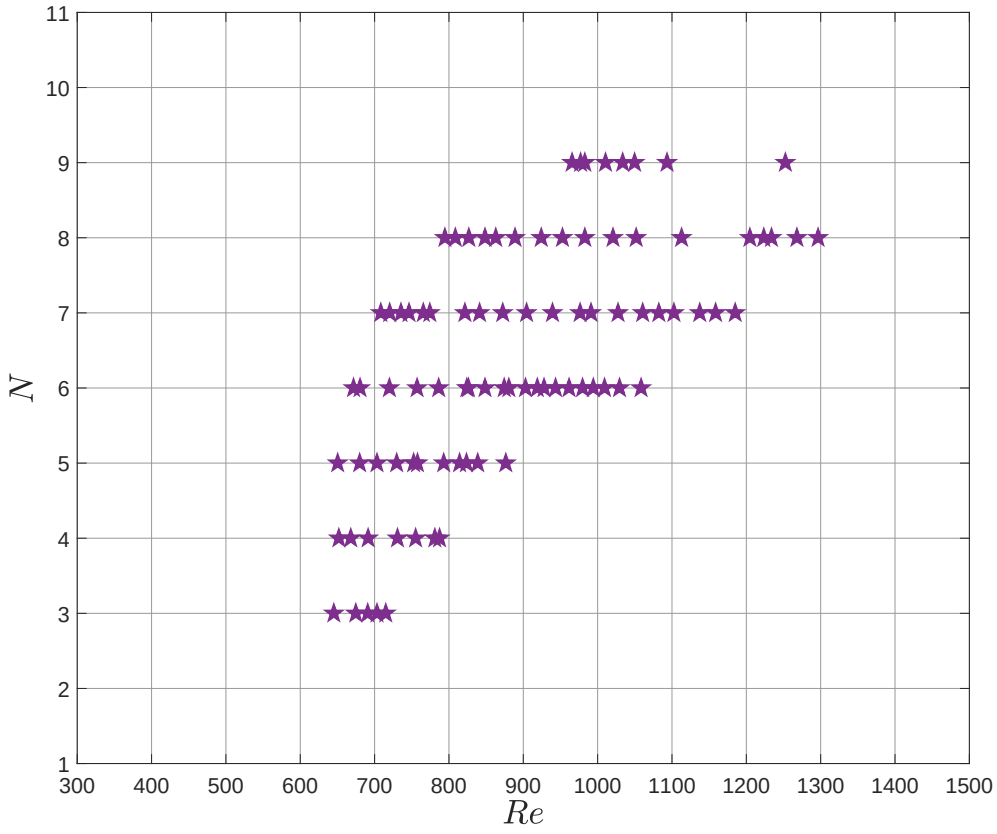

Figure 3.5: Mode number N against Reynolds number for the $h_w = 3.4$mm weir on the $r_w = 17.8$cm plate for forced experiments.

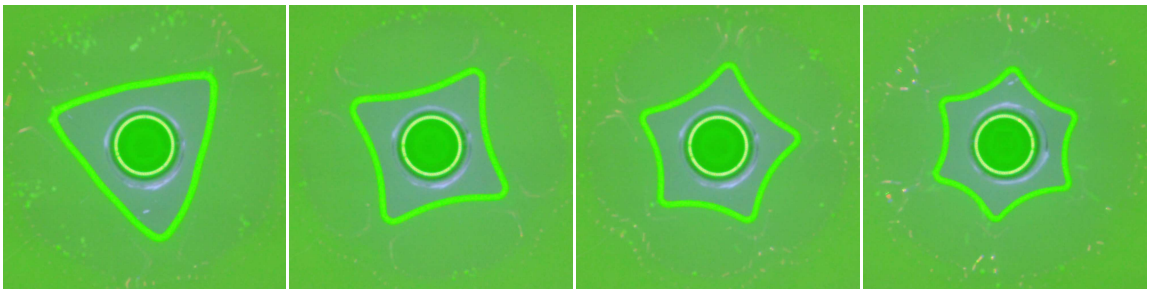

Figure 3.6: Modes $N = 3 - 6$ exist for a Reynolds number $Re = 690$ using the forced method.

3.2 Geometry of the jump A/PH

As shown above, the experimental protocol is important in mode number selection. Each polygonal shape is characterized by a mode number N, area A, perimeter P and external height H. For a fixed height weir, we take the data shown in Figures 3.2 and 3.3 from the natural and upscale-downscale protocols, respectively, and compute the characteristic ratio A/PH. Figure 3.7 plots that data against Reynolds number Re which shows a collapse of the data indicating that the particular experimental protocol is unimportant in determining this ratio. This observation perhaps goes against intuition in which one might expect the A/PH ratio for a $N = 7$ and $N = 9$ mode to be different for a fixed Reynolds number $Re = 930$ (cf. Figure 3.3). This collapse also occurs for other fixed height weirs but along a different curve.

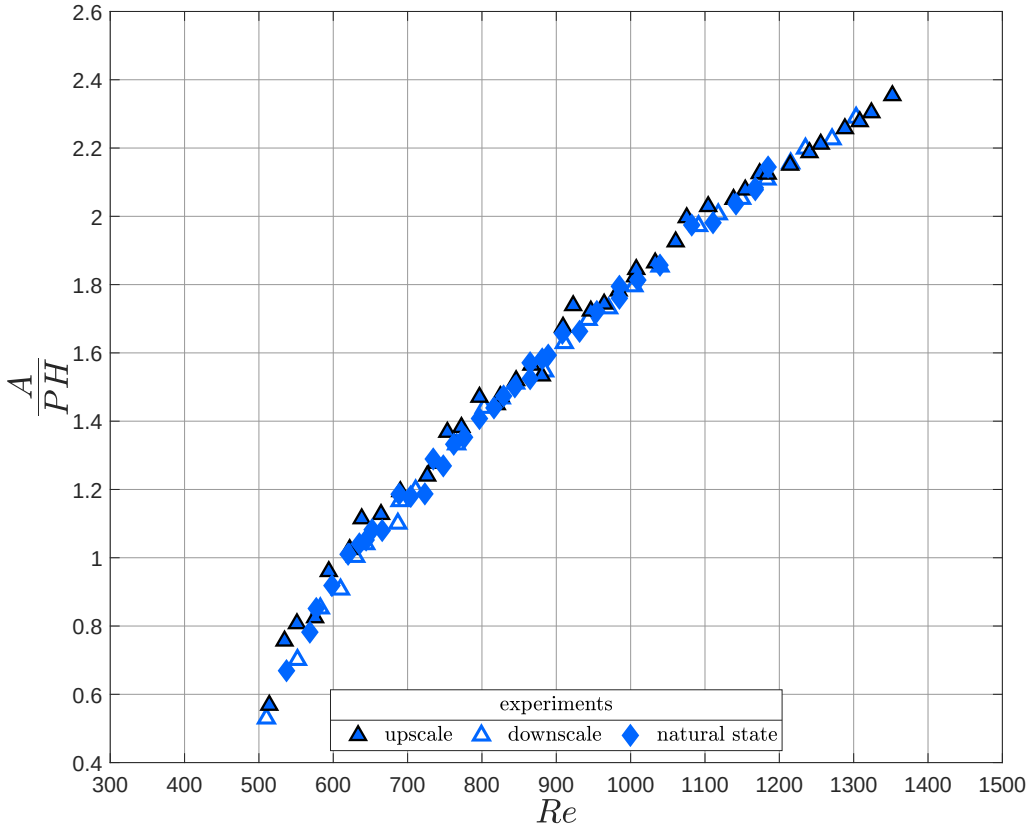

Figure 3.7: Characteristic ratio A/PH against Reynold's number Re for the $3.17mm$ weir on the circular plate with radius $17.8cm$ contrasting the natural state and upscale-downscale protocols.

3.3 The effect of weir geometry and height

3.3.1 Varying height H

Mode number selection and the characteristic ratio A/PH are affected by the weir geometry and height. Figure 3.8 plots the hysteresis ΔRe against mode number N, as it depends upon the weir height h_w. Modes $N = 3 - 6$ generally share the same trend, but at $N = 7$ the taller weirs begin to deviate from the shorter weirs and exhibit large hysteresis. This is most likely related to the higher relative inertia Re required to create such shapes.

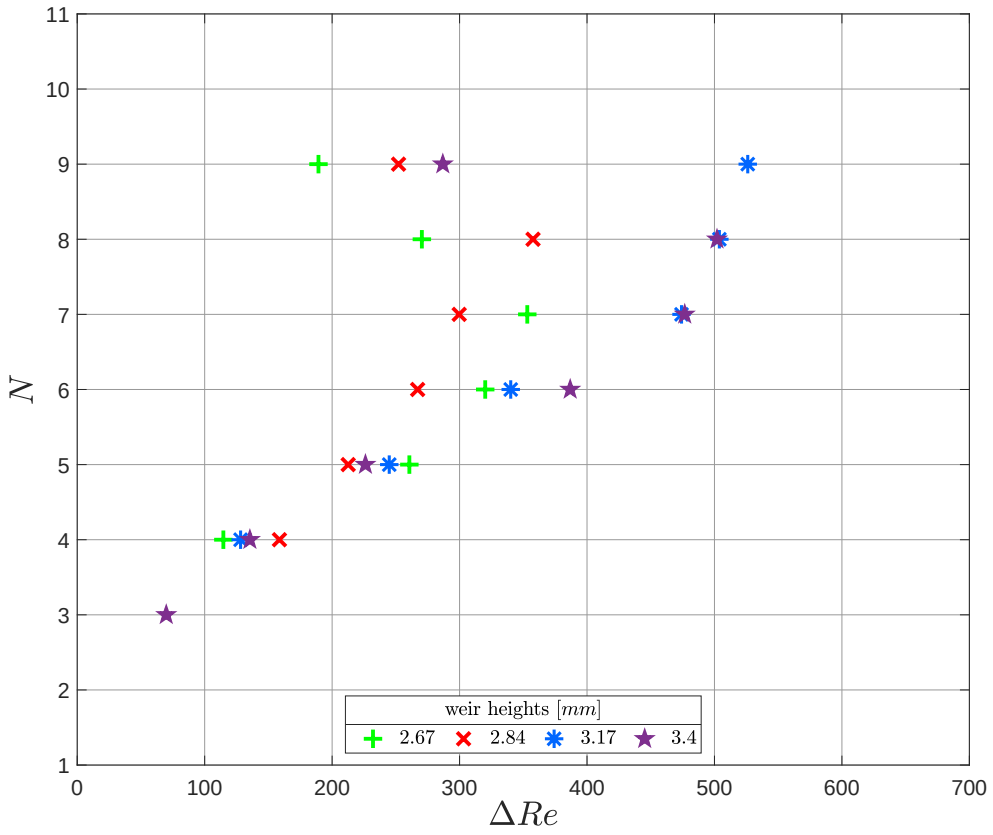

Figure 3.8: Mode number N against hysteresis ΔRe as it depends upon weir height h_w on the 17.8cm plate for the upscale-downscale protocol. The weir heights h_w are denoted differently. See figure 3.3 on a visual on calculating delta Reynold's number ΔRe

Figure 3.9 plots the characteristic ratio A/PH against Reynolds number Re as it depends upon the weir height h_w and shows the curve shifts to the right for increasing weir height. That is,

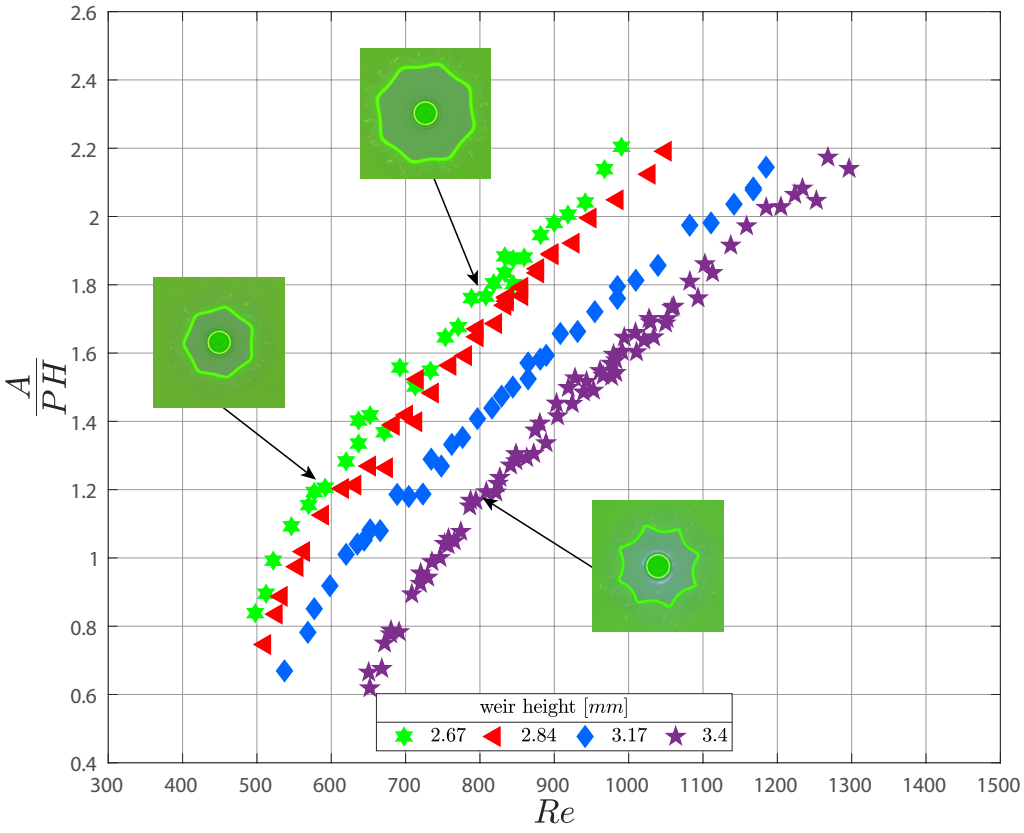

Figure 3.9: Characteristic ratio A/PH against Reynolds number Re as it depends upon weir height h_w for the $r_w = 17.78$cm plate. Weirs $h_w = 2.67\text{mm}, 2.84\text{mm}, 3.17\text{mm}$ include natural state data, and weir $h_w = 3.4$mm includes forced data. For a Reynolds number $Re = 800$, the $N = 8$ mode shows a dramatic difference between the $h_w = 2.67$mm and $h_w = 3.4$mm weirs.

more inertia is required to create a shape with identical A/PH for taller weirs. For a fixed $Re = 800$, the shapes vary dramatically between different weir heights. Figure 3.9 (inset) shows the shapes become more concave a the weir height increases. For fixed $A/PH = 1.2$, the mode number N increases with Re and the shape becomes more concave. We include the forced data $h_w = 3.4$mm in Figure 3.9 to show it follows similar trends as the other weirs.

3.3.2 Varying weir geometry

We are interested in the effect of weir geometry and investigate by varying the weir radius from $r_w = 7.62 - 17.2$cm for a fixed weir height. We also tried using a square weir with edge length

22cm.

Figure 3.10 plots the mode number N against Reynolds number Re for our three largest radius weirs at a fixed height using the upscale-downscale protocol. As shown, the data is similar for each weir radius and the modal transitions happen at approximately the same Re within a few mL/s. Figure 3.11 plots the hysteresis ΔRe against mode number N from Figure 3.10 which is shown to not depend upon the weir radius for the three largest circular weirs. The greatest difference occurs for the $N = 9$ mode and is $\approx 7.5m$L/s. We attribute these small differences to experimental error and conclude that weir radius does not affect mode number selection for the three largest radii weirs.

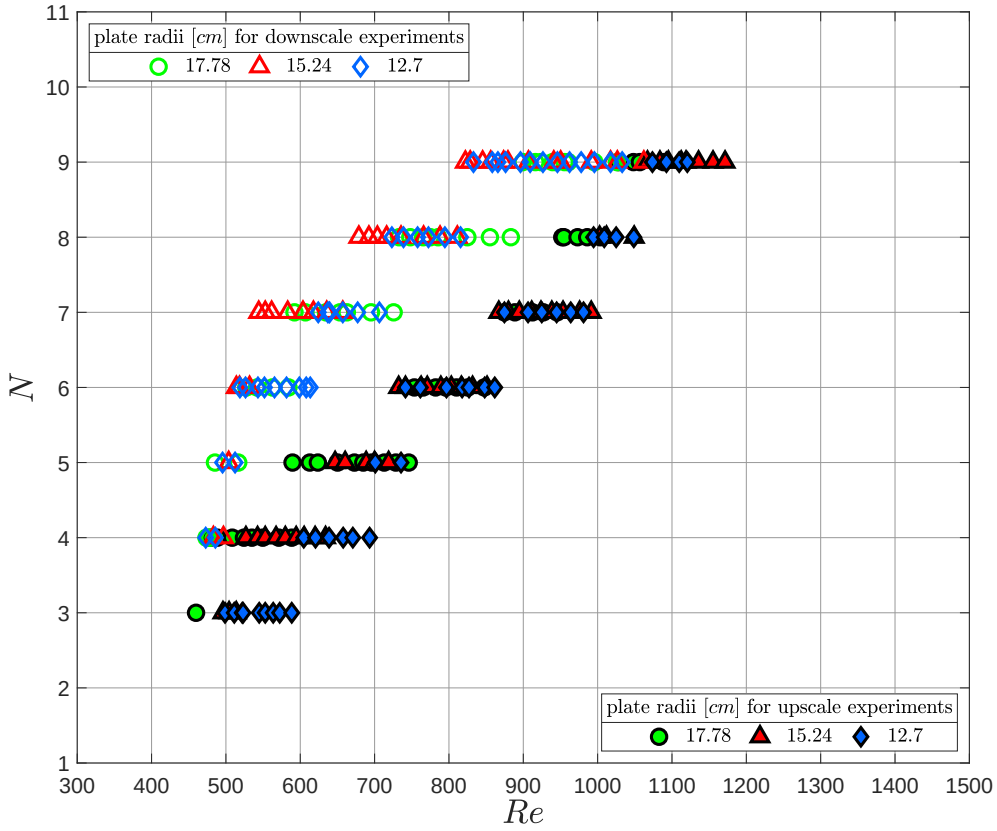

Figure 3.10: Mode number N against Reynolds number Re for the $h_w = 2.84$mm as it depends upon the weir radius for the upscale and downscale experiments.

A similar trend is seen in the natural state protocol, as shown in Figure 3.12 which plots the mode number N against Reynolds number Re. The data from the three largest radius circular weirs overlay one another up to experimental error. We also include data from the square weir with

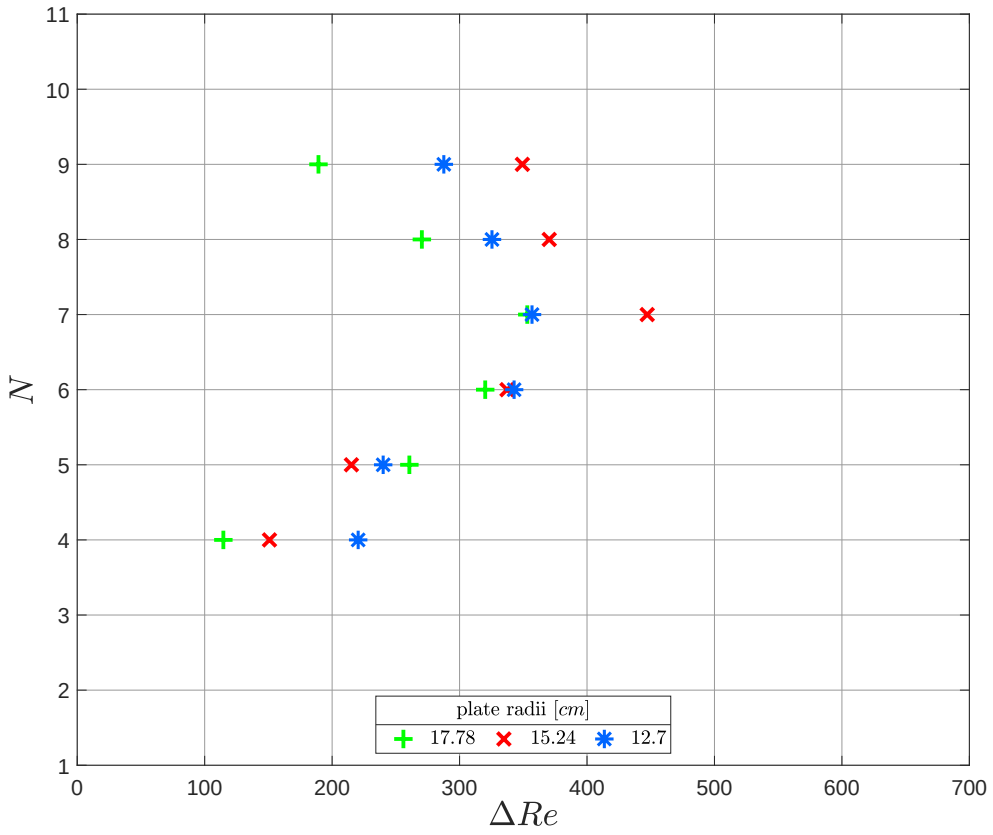

Figure 3.11: Mode number N against hysteresis ΔRe for the $h_w = 2.84$mm weir as it depends upon the weir geometry for the upscale and downscale experiments.

edge length 22cm and identical height, which is shifted towards higher Reynolds number indicating that more inertia is required to create a given mode shape. This is our first observation that weir geometry can affect mode number selection in polygonal hydraulic jumps. Similar conclusions can be made for weirs with other heights. Even though mode number selection differs with the square plate geometry, the characteristic ratio is unaffected, as shown in Figure 3.13 which shows a collapse of the data irrespective of weir geometry. Recall that weir height will affect this curve.

Thus far, multiple weir geometries have been used and only the square weir showed deviation in results from the other circular geometries. To further investigate, we use a significantly smaller radius $r_w = 7.62$cm weir and conduct both natural state and upscale-downscale experiments. Figure 3.14 plots the mode number N against Reynolds number Re for the upscale-downscale experiments for the smallest $r_w = 7.62$cm and largest $r_w = 17.2$cm radius weir. It is interesting to note that the

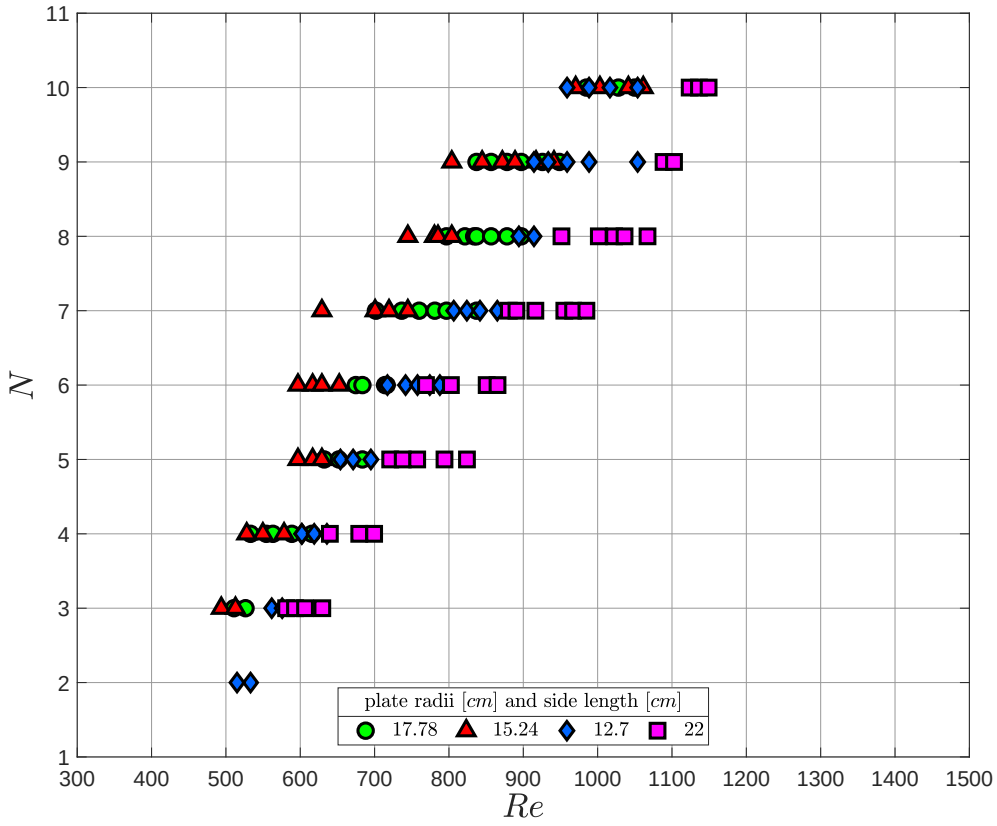

Figure 3.12: Mode number N against Reynolds number Re for the $h_w = 2.84$mm weir as it depends upon the weir geometry for natural state experiments.

downscale sweep is relatively unaffected by weir radius, however the upscale sweep shows a dramatic difference with the smaller radius weir exhibiting a modal transition at much smaller Reynolds number than the largest radius weir. This difference is more significant than experimental error and suggests weir radius plays a role when the scale of the jump becomes comparable in magnitude to the scale of the weir. For all other cases, the jump radius was significantly smaller than the weir radius. This implies that the flow field at a certain distance downstream from the hydraulic jump does not affect the jump itself.

Though stable hydraulic jumps can be accomplished with a smaller geometry plate, it is important to note that weir geometry can affect the behavior and structure. We observed that with a weir to nozzle radius ratio $r_w/r_N \geq 28$ the results are indistinguishable. While those with $r_w/r_N \approx 16.5$ they are noticeably different.

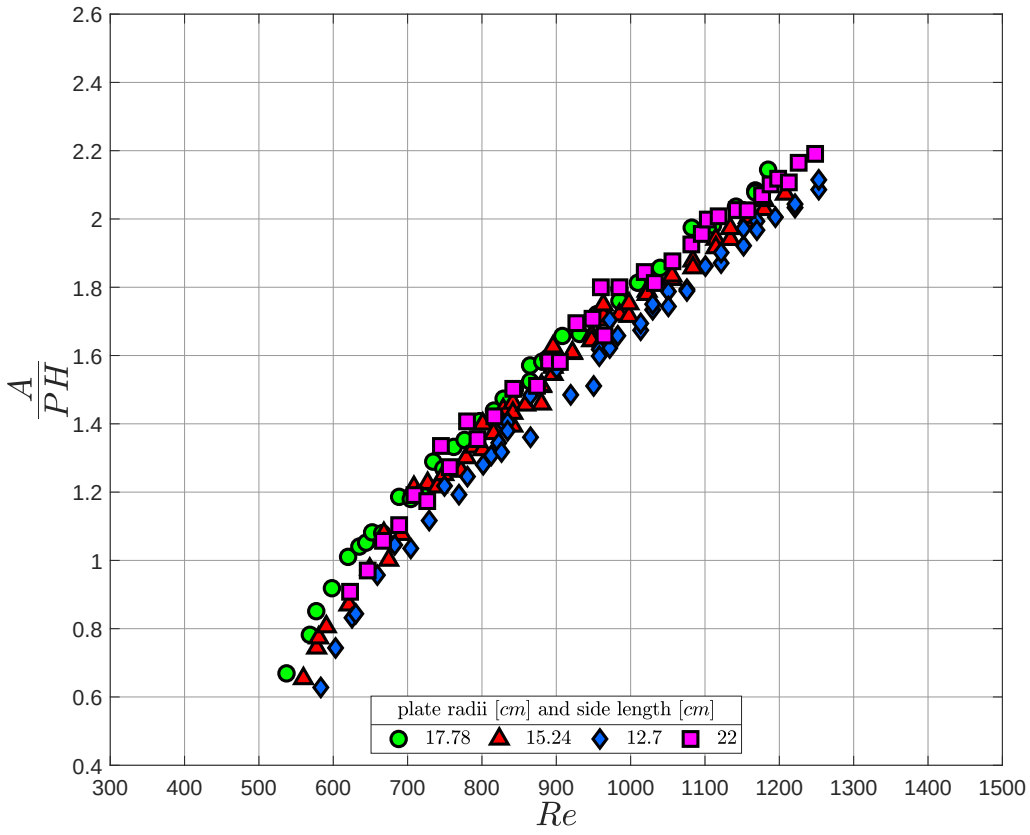

Figure 3.13: Characteristic ratio A/PH against Reynolds number Re for the $h_w = 3.17$mm weir as it depends upon the weir geometry.

3.3.3 Collapsing the data

As discussed in the previous sections, the characteristic ratio A/PH is independent of the mode number N and experimental protocol for a fixed weir height h_w. For each h_w, there is a different trend, as shown in Figure 3.9, demonstrating that A/PH is dependent upon H of the flow. We scale the external height H with the perimeter P of the polygonal jumps and plot that result against the downstream Weber number in Figure 3.15. The data collapses for all weir heights and geometries used here. This suggests that the downstream fluid height H should be used as the characteristic length scale in describing polygonal hydraulic jumps.

It's notable that with the same y-axis values the data does not collapse using the jet Reynold's number Re. This implies that for fixed fluid properties that flow rate Q and external

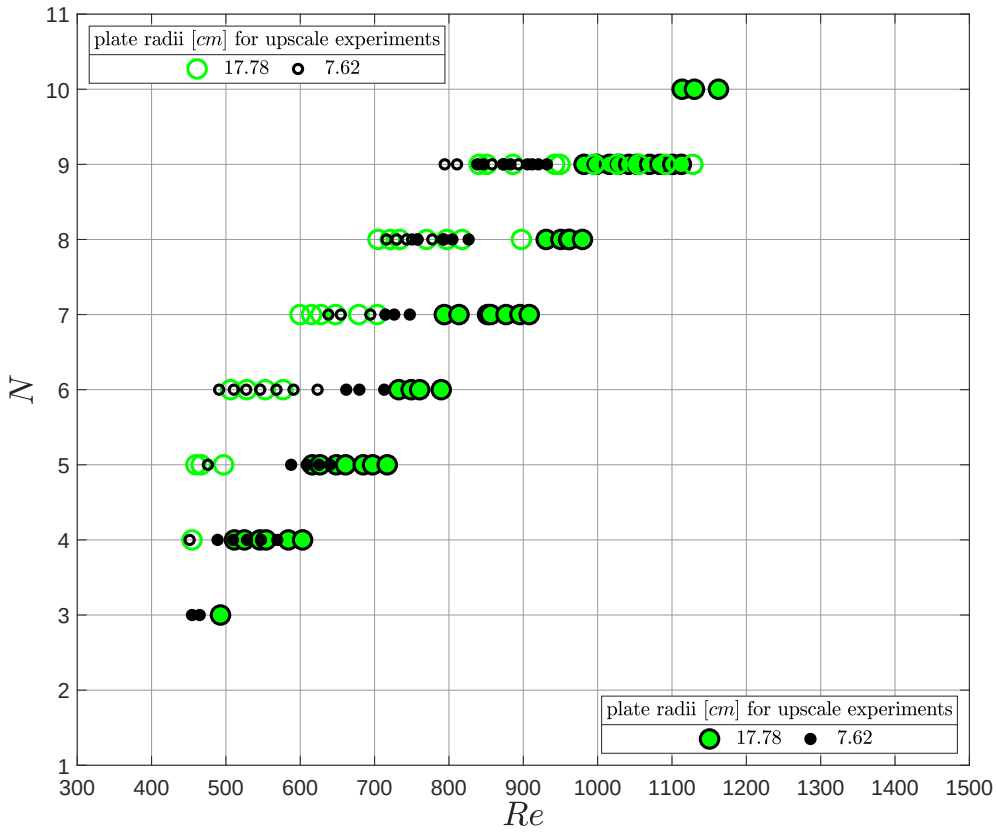

Figure 3.14: Mode number N against jet Reynolds number Re for the $h_w = 2.84$mm weir on the circular plates with smallest $r_w = 7.62$cm and largest $r_w = 17.8$cm radius for the upscale and downscale experiments.

height H uniquely determine the area A and perimeter P irrespective of mode number N, weir geometry or experimental protocol.

3.3.4 Critical wavelength and connection to Plateau-Rayleigh breakup

We examine the scaled wavelength λ/H as a function of mode number N in Figure 3.16 for the upscale-downscale protocol and Figure 3.17 for the natural state protocol. Were the wavelength $\lambda = P/N$. Figure 3.16 shows a larger wavelength for the upscale sweep and the wavelength difference between upscale and downscale decreases with increasing mode number N. This random spread seen in the upscale data in Figure 3.16 could be explained by the asymmetric behavior (Fig. 3.4a). Looking at Figure 3.9 the P for $h_w = 2.67$mm increases at slower rate than the 3.17mm weir, and

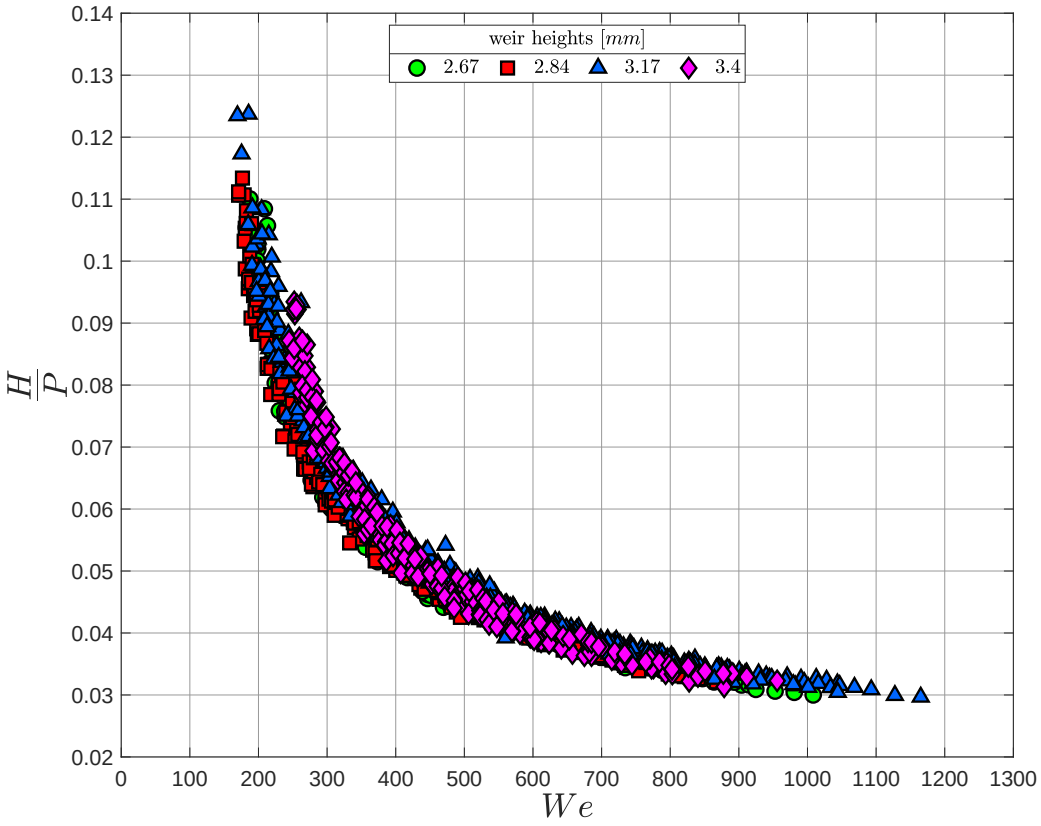

Figure 3.15: Weber number We against H/P for all data.

since the λ/H transition during the downscale for the $h_w = 2.67$mm & 2.84mm weirs is higher than the $h_w = 3.17$mm weirs, this would follow the data. These results also suggest that the critical wavelength for the $(N \to N-1)$ and $(N \to N+1)$ transitions is not solely related to the height of the fluid. Figure 3.17 shows the wavelength is a slowly decreasing function of mode number N whose average value is approximately $\lambda/H \approx 3$. Weir height does not seem to affect the scaled wavelength. This approximately constant value is consistent with the Plateau-Rayleigh instability mechanism where the critical scaled wavelength is constant and depends upon the radius of the cylinder, which would correlate to the fluid height H in our toroidal geometry.

Although the λ/H ratio curve changes with weir height h_w, as shown in Figure 3.17, the fact that λ/H does not change with h_w suggests that the wavelength selection mechanism is robust suggesting the Plateau-Rayleigh instability as a logical mechanism in describing the polygonal jump

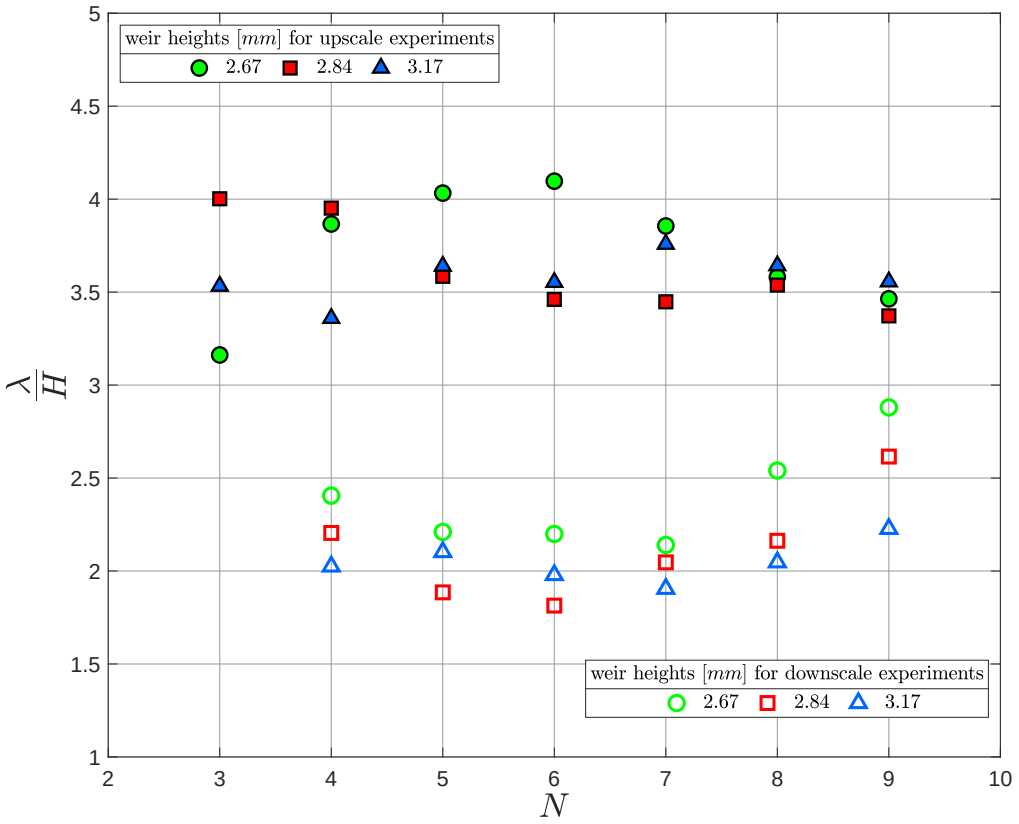

Figure 3.16: Mode number N against scaled wavelength λ/H as it depends upon weir height h_w on the $r_w = 17.8$cm plate for the upscale and downscale experiments.

geometry. The small deviation of λ/H with mode number N suggests a weak dependence upon another parameter, which might include the secondary curvature of the toroidal shape which becomes more important for smaller mode numbers. This interpretation is consistent with our results shown in Figure 3.17.

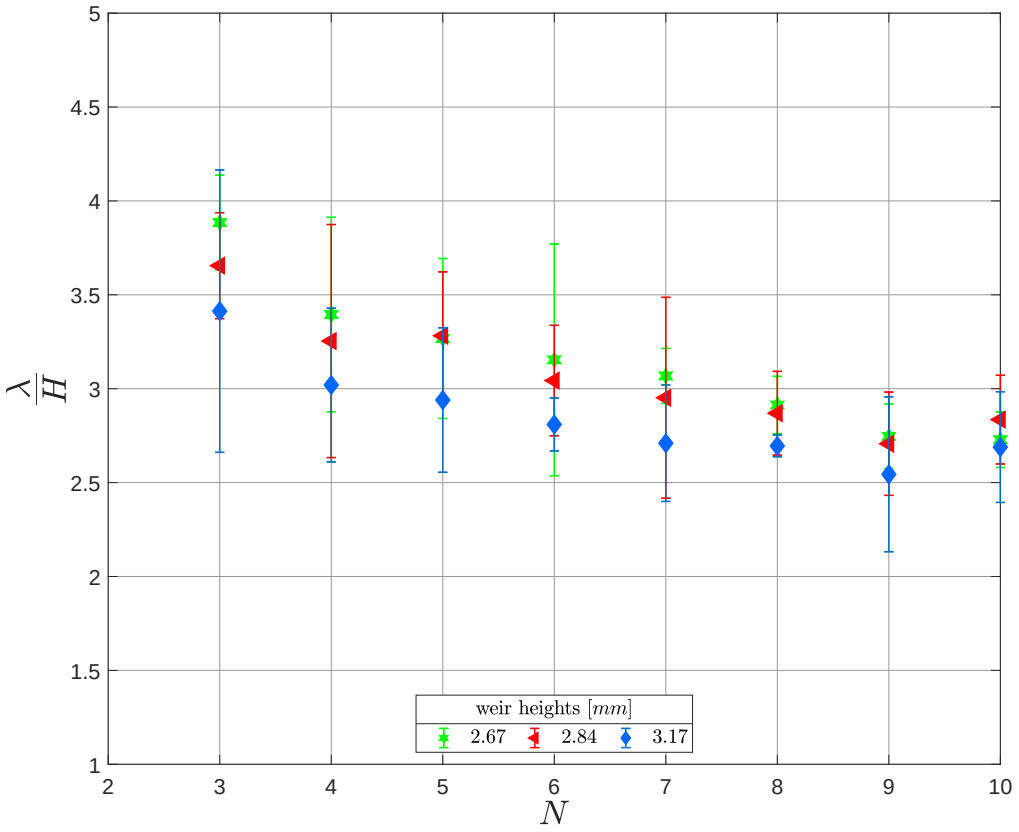

Figure 3.17: Scaled wavelength λ/H against mode number N as it depends upon weir height h_w on the $r_w = 17.8$cm plate for the natural state experiments.

Chapter 4

Discussion

In previous experiments involving polygonal hydraulic jumps [16, 17, 12, 49] information regarding the weir geometry and the experimental protocol has not been reported in great detail, thus hindering repeatability in experiment, as well as interpreting those results. We have explicitly addressed these shortcomings through careful documentation of the experimental setup and protocol. This information can be used to improve mathematical models. For example, the model of Rojas [46, 45, 44] requires an explicit knowledge of the downstream boundary conditions (fluid height, weir height, etc.) in order to predict modal behavior. We have documented that modal behavior is affected by the experimental protocol, as contrasted by the upscale-downscale and natural state protocols. In the upscale-downscale experiments, the hysteresis range ΔRe is identified for weirs showing the hysteresis ΔRe dramatically increases with weir height. Hysteresis is also seen to increase with mode number N which implies that the mode selection mechanism is inherently nonlinear and any such future model would need to incorporate hysteresis to properly predict modal behavior.

It is not possible to physically measure the geometry (perimeter, area) of the polygonal hydraulic jump. Previous authors have attempted to average the inner and outer radii in order to estimate the jump geometry but this introduces error into a process which is known to be extremely sensitive to small changes in the jump geometry. Image processing methods are used to extract the area A and perimeter P of these structures revealing new information that can be useful in understanding the physics of the polygonal hydraulic jump as well as for future models. We have shown the characteristic ratio A/PH is set by the Reynolds number Re and does not depend on

flow history or mode number N. However, the ratio does depend upon the weir height h_w and we show that in order to achieve a similar jump geometry it requires more inertia as measured by the increasing Reynolds number. All of our data collapses upon scaling with the downstream Weber number indicating that the downstream height H is the relevant length scale in this problem. This implies the polygonal hydraulic jump phenomenon is purely geometric.

By scaling the wavelength λ with external fluid height H and plotting against modes N, a collapse of the data is seen illustrating the modal selection mechanism is similar to the Plateau-Rayleigh instability of a liquid column, which exhibits a constant scaled wavelength λ/H irrespective of mode. Our scaled wavelength $\lambda/H = 3$, which differs from the Plateau-Rayleigh prediction of $\lambda/H = 4.5$ and we attribute this difference to a number of factors that influence this constant, such as the introduction of a secondary curvature in the toroidal geometry compared to the cylinder and the role of viscosity in defining the critical wavelength. This shift in critical wavelength is also seen in Plateau-Rayleigh breakup of liquid rivulets [7]. Rotating vortexes under the jump interface, the imperfect curvature at the jump interface, and flow downstream of the jump could also play a role. As mentioned by Pairam 2009 [37], for a torodial donut the major and minor radii alter from an initial shape by expanding or contracting the donut until a critical value is reached upon which the donut pinches off in the critical wavelength. Note that the hydraulic jump geometry is unable to spontaneously expand or contract like in [37] to adopt a preferred geometry and perhaps for this reason there is a range of preferred λ/H the we see in experiment. This is best seen in the upscale-downscale experiments which exhibit different critical wavelengths for the maximum and minimum modes. Even so, there is a mild collapse of the data for these states indicating that polygonal hydraulic jumps are a geometric phenomena governed by a complex balance between surface tension, viscosity and fluid inertia.

Chapter 5

Conclusion

An experimental apparatus was constructed and approximately 1800 observations of polygonal hydraulic jumps were made. Diagnostic techniques and image processing protocols allowed characterization of the geometry of the polygonal jump through the mode number N, perimeter P, area A and downstream fluid height H. Three experimental protocols are developed; natural state, upscale-downscale and forced, and we characterize the modal transition for each. With regard to the upscale-downscale protocol, the transition in the upscale sweep $N \rightarrow N+1$ typically happens when the sides of the become convex or the polygon asymmetric, whereas on the downscale sweep all sides are concave and the transition happens at similar scaled wavelength λ/H. This typically happens when the rotating vortexes in the corners start to interfere with each other. The robustness for each mode N is defined by the hysteresis ΔRe and the modes $N = 3-5$ have nearly identical ΔRe irrespective of weir height. Natural state experiments identify the optimal mode number N for each Reynolds number Re but this is not necessarily unique and multiple modes can exist at a give Re. Although mode number selection is affected by the experimental protocol, we show that the characteristic ratio A/PH does not and yields a unique curve for each weir height h_w. Weir geometry does not affect mode selection unless the ratio of weir radius to nozzle radius is less than $r_w/r_N < 17$. All of our data collapses upon scaling with the downstream Weber number suggesting the downstream fluid height is the proper choice of length scale in this problem. Lastly, we show the scaled wavelength λ/H approaches a constant value suggesting the instability mechanism is related to Plateau-Rayleigh breakup. All of our observations allows us to better understand the fluid mechanics behind mode selection and the geometry of polygonal hydraulic jumps.

Chapter 6

Bibliography

[1] CT Avedisian and Z Zhao. The circular hydraulic jump in low gravity. In *Proceedings of the Royal Society of London A: Mathematical, Physical and Engineering Sciences*, volume 456, pages 2127–2151. The Royal Society, 2000.

[2] Jeffrey M Bergthorson, Kazuo Sone, Trent W Mattner, Paul E Dimotakis, David G Goodwin, and Dan I Meiron. Impinging laminar jets at moderate reynolds numbers and separation distances. *Physical Review E*, 72(6):066307, 2005.

[3] Garrett Birkhoff, EH Zarantonello, and Wakes Jets. Cavities. *New York*, 1957.

[4] Tomas Bohr, Peter Dimon, and Vakhtang Putkaradze. Shallow-water approach to the circular hydraulic jump. *Journal of Fluid Mechanics*, 254:635–648, 1993.

[5] Tomas Bohr, Vachtang Putkaradze, and Shinya Watanabe. Averaging theory for the structure of hydraulic jumps and separation in laminar free-surface flows. *Physical review letters*, 79(6): 1038, 1997.

[6] Tomas Bohr, C Ellegaard, A Espe Hansen, K Hansen, A Haaning, V Putkaradze, and S Watanabe. Separation and pattern formation in hydraulic jumps. *Physica A: Statistical Mechanics and its Applications*, 249(1-4):111–117, 1998.

[7] JB Bostwick and PH Steen. Static rivulet instabilities: varicose and sinuous modes. *Journal of Fluid Mechanics*, 837:819–838, 2018.

[8] Mustapha Bouhadef. Étalement en couche mince d'un jet liquide cylindrique vertical sur un plan horizontal. *Zeitschrift für angewandte Mathematik und Physik ZAMP*, 29(1):157–167, 1978.

[9] RI Bowles and FT Smith. The standing hydraulic jump: theory, computations and comparisons with experiments. *Journal of Fluid Mechanics*, 242:145–168, 1992.

[10] Y Brechet and Z Neda. On the circular hydraulic jump. *American Journal of Physics*, 67(8): 723–731, 1999.

[11] John WM Bush and Jeffrey M Aristoff. The influence of surface tension on the circular hydraulic jump. *Journal of Fluid Mechanics*, 489:229–238, 2003.

[12] John WM Bush, Jeffrey M Aristoff, and AE Hosoi. An experimental investigation of the stability of the circular hydraulic jump. *Journal of Fluid Mechanics*, 558:33–52, 2006.

[13] ADD Craik, RC Latham, MJ Fawkes, and PWF Gribbon. The circular hydraulic jump. *Journal of Fluid Mechanics*, 112:347–362, 1981.

[14] Emilie Dressaire, Laurent Courbin, Jérome Crest, and Howard A Stone. Thin-film fluid flows over microdecorated surfaces: Observation of polygonal hydraulic jumps. *Physical Review Letters*, 102(19):194503, 2009.

[15] F Durst, S Ray, B Ünsal, and OA Bayoumi. The development lengths of laminar pipe and channel flows. *Journal of fluids engineering*, 127(6):1154–1160, 2005.

[16] Clive Ellegaard, Adam Espe Hansen, Anders Haaning, and Tomas Bohr. Experimental results on flow separation and transitions in the circular hydraulic jump. *Physica Scripta*, 1996(T67): 105, 1996.

[17] Clive Ellegaard, Adam Espe Hansen, Anders Haaning, Kim Hansen, Anders Marcussen, Tomas Bohr, Jonas Lundbek Hansen, and Shinya Watanabe. Creating corners in kitchen sinks. *Nature*, 392(6678):767, 1998.

[18] Clive Ellegaard, Adam Espe Hansen, Anders Haaning, Kim Hansen, Anders Marcussen, Tomas Bohr, Jonas Lundbek Hansen, and Shinya Watanabe. Cover illustration: Polygonal hydraulic jumps. *Nonlinearity*, 12(1):1, 1999.

[19] Mario Errico. *A study of the interaction of liquid jets with solid surfaces*. 1986.

[20] Valdemir Garcia Ferreira, Murilo Francisco Tomé, Norberto Mangiavacchi, A Castelo, José Alberto Cuminato, Armando de Oliveira Fortuna, and Sean Mckee. High-order upwinding and the hydraulic jump. *International journal for numerical methods in fluids*, 39(7):549–583, 2002.

[21] FJ Higuera. The hydraulic jump in a viscous laminar flow. *Journal of fluid Mechanics*, 274: 69–92, 1994.

[22] FJ Higuera. The circular hydraulic jump. *Physics of Fluids*, 9(5):1476–1478, 1997.

[23] Seikan Ishigai, Shigeyasu NAKANISHI, Minoru MIZUNO, and Toyoo IMAMURA. Heat transfer of the impinging round water jet in the interference zone of film flow along the wall. *Bulletin of JSME*, 20(139):85–92, 1977.

[24] Gilles Jannes, Robert Piquet, Philippe Maïssa, Christian Mathis, and G Rousseaux. Experimental demonstration of the supersonic-subsonic bifurcation in the circular jump: A hydrodynamic white hole. *Physical Review E*, 83(5):056312, 2011.

[25] Thomas RN Jansson, Martin P Haspang, Kåre H Jensen, Pascal Hersen, and Tomas Bohr. Polygons on a rotating fluid surface. *Physical review letters*, 96(17):174502, 2006.

[26] M Johnson, D Maynes, and J Crockett. Experimental characterization of hydraulic jump caused by jet impingement on micro-patterned surfaces exhibiting ribs and cavities. *Experimental Thermal and Fluid Science*, 58:216–223, 2014.

[27] Aslan R Kasimov. A stationary circular hydraulic jump, the limits of its existence and its gasdynamic analogue. *Journal of Fluid Mechanics*, 601:189–198, 2008.

[28] RP Kate, PK Das, and Suman Chakraborty. Hydraulic jumps due to oblique impingement of circular liquid jets on a flat horizontal surface. *Journal of Fluid Mechanics*, 573:247–263, 2007.

[29] RP Kate, PK Das, and Suman Chakraborty. Investigation on non-circular hydraulic jumps formed due to obliquely impinging circular liquid jets. *Experimental Thermal and Fluid Science*, 32(8):1429–1439, 2008.

[30] Matthieu Labousse and John WM Bush. The hydraulic bump: The surface signature of a plunging jet. *Physics of Fluids*, 25(9):229–238, 2013.

[31] Matthieu Labousse and John WM Bush. Polygonal instabilities on interfacial vorticities. *The European Physical Journal E*, 38(10):113, 2015.

[32] X Liu and JH Lienhard. The hydraulic jump in circular jet impingement and in other thin liquid films. *Experiments in Fluids*, 15(2):108–116, 1993.

[33] Erik A Martens, Shinya Watanabe, and Tomas Bohr. Model for polygonal hydraulic jumps. *Physical Review E*, 85(3):036316, 2012.

[34] MJ McCarthy and NA Molloy. Review of stability of liquid jets and the influence of nozzle design. *The Chemical Engineering Journal*, 7(1):1–20, 1974.

[35] VE Nakoryakov, BG Pokusaev, and EN Troyan. Impingement of an axisymmetric liquid jet on a barrier. *International Journal of Heat and Mass Transfer*, 21(9):1175–1184, 1978.

[36] RG Olsson and ET Turkdogan. Radial spread of a liquid stream on a horizontal plate. *Nature*, 211(5051):813, 1966.

[37] E Pairam and A Fernández-Nieves. Generation and stability of toroidal droplets in a viscous liquid. *Physical review letters*, 102(23):234501, 2009.

[38] Mohammad Passandideh-Fard, Ali Reza Teymourtash, and Mohammad Khavari. Numerical study of circular hydraulic jump using volume-of-fluid method. *Journal of Fluids Engineering*, 133(1):011401, 2011.

[39] Joseph Plateau. *Statique expérimentale et théorique des liquides soumis aux seules forces moléculaires*, volume 2. Gauthier-Villars, 1873.

[40] A Rao and JH Arakeri. Wave structure in the radial film flow with a circular hydraulic jump. *Experiments in Fluids*, 31(5):542–549, 2001.

[41] Arnab K Ray and Jayanta K Bhattacharjee. Standing and travelling waves in the shallow-water circular hydraulic jump. *Physics Letters A*, 371(3):241–248, 2007.

[42] Lord Rayleigh. On the capillary phenomena of jets. *Proc. R. Soc. London*, 29(196-199):71–97, 1879.

[43] Lord Rayleigh. On the theory of long waves and bores. *Proceedings of the Royal Society of London. Series A, Containing Papers of a Mathematical and Physical Character*, 90(619): 324–328, 1914.

[44] N Rojas and E Tirapegui. Harmonic solutions for polygonal hydraulic jumps in thin fluid films. *Journal of Fluid Mechanics*, 780:99–119, 2015.

[45] N Rojas, M Argentina, and E Tirapegui. A progressive correction to the circular hydraulic jump scaling. *Physics of Fluids*, 25(4):042105, 2013.

[46] NO Rojas, M Argentina, E Cerda, and E Tirapegui. Inertial lubrication theory. *Physical review letters*, 104(18):187801, 2010.

[47] Ahmad Saberi, Mohammad Reza Mahpeykar, and Ali Reza Teymourtash. Experimental measurement of radius of circular hydraulic jumps: Effect of radius of convex target plate. *Flow Measurement and Instrumentation*, 65:274–279, 2019.

[48] Itiro Tani. Water jump in the boundary layer. *Journal of the Physical Society of Japan*, 4(4-6): 212–215, 1949.

[49] Ali Reza Teymourtash and Mohsen Mokhlesi. Experimental investigation of stationary and rotational structures in non-circular hydraulic jumps. *Journal of Fluid Mechanics*, 762:344–360, 2015.

[50] Ali Reza Teymourtash, Mohammad Khavari, and Mohammad Passandideh Fard. Experimental and numerical investigation of circular hydraulic jump. In *ISME2010*, 2010.

[51] Vittal Krishnamurthy Vasista et al. *Experimental study of the hydrodynamics of an impinging liquid jet*. PhD thesis, Massachusetts Institute of Technology, 1989.

[52] Yunpeng Wang and Roger E Khayat. The role of gravity in the prediction of the circular hydraulic jump radius for high-viscosity liquids. *Journal of Fluid Mechanics*, 862:128–161, 2019.

[53] Shinya Watanabe, Vachtang Putkaradze, and Tomas Bohr. Integral methods for shallow free-surface flows with separation. *Journal of Fluid Mechanics*, 480:233–265, 2003.

[54] EJ Watson. The radial spread of a liquid jet over a horizontal plane. *Journal of Fluid Mechanics*, 20(3):481–499, 1964.

[55] Kensuke Yokoi and Feng Xiao. A numerical study of the transition in the circular hydraulic jump. *Physics Letters A*, 257(3-4):153–157, 1999.

[56] Kensuke Yokoi and Feng Xiao. Relationships between a roller and a dynamic pressure distribution in circular hydraulic jumps. *Physical Review E*, 61(2):R1016, 2000.

[57] Kenuke Yokoi and Feng Xiao. Mechanism of structure formation in circular hydraulic jumps: Numerical studies of strongly deformed free-surface shallow flows. *Physica D: Nonlinear Phenomena*, 161(3-4):202–219, 2002.

[58] Jiangang Zhao and Roger E Khayat. Spread of a non-newtonian liquid jet over a horizontal plate. *Journal of Fluid Mechanics*, 613:411–443, 2008.